PROCEEDINGS, 43rd Workshop on Geothermal Reservoir Engineering
Stanford University, Stanford, California, February 12-14, 2018
SGP-TR-213

Exploring the Role of Mixed-Mechanism Fracturing and Fluid-Faulting Interactions During the 2014 Long Valley Caldera, California, Earthquake Swarm

Jack H. Norbeck[1] and David R. Shelly[2]

[1]Earthquake Science Center, U.S. Geological Survey, 345 Middlefield Rd., Menlo Park, California, USA 94025

[2]Volcano Science Center, U.S. Geological Survey, 345 Middlefield Rd., Menlo Park, California, USA 94025

Corresponding author email: jnorbeck@usgs.gov

Keywords: mixed-mechanism fracturing, earthquake swarms, earthquake hazard, volcano hazard

ABSTRACT

Several sequences of intense earthquake swarm activity occurred beneath the Long Valley Caldera between May and November 2014. At the height of swarm on September 26, three magnitude 3.5 events occurred within a matter of hours. The swarm has been proposed to result from an interaction between aqueous fluid, a product of the underlying volcanic system, and dominantly tectonic stress. To explore this hypothesis, we performed a stress inversion based on a high-resolution catalog of earthquake locations and focal mechanisms. We determined that the orientation of the minimum principal stress was well-constrained to be subhorizontal at an azimuth of roughly 225° to 245°. The principal coordinate system is oriented close to the vertical and horizontal directions. Assuming a vertical stress gradient of 25 MPa/km, the minimum and maximum horizontal stress magnitudes were estimated to range from 15.1 to 18.3 MPa/km and from 26.0 to 36.0 MPa/km, respectively. The mixture of both strike-slip and normal faulting focal mechanism solutions suggests that the magnitude of intermediate and maximum principal stresses are similar to each other, indicating that the maximum horizontal stress is likely to be toward the lower end of the range estimated from the stress inversion.

We integrated the results of the stress inversion with the fault structure geometry inferred from the relocated seismicity and focal mechanism catalogs to develop a three-dimensional hydromechanical model of the Long Valley Caldera site. Our numerical simulations were aimed at identifying fluid-faulting interactions that may have controlled the swarm activity. In particular, we investigated the hypothesis that fluid overpressure events caused the formation of hydraulic splay fractures to occur in bursts such that fluid migrated through both preexisting and newly formed fractures in a mixed-mechanism process. We found that our modeling results were consistent with the observed earthquake sequence behavior, suggesting that mixed-mechanism fracturing may have been the process controlling fluid-faulting interactions during the swarm.

1. INTRODUCTION

Long Valley Caldera formed ~767 ka in the cataclysmic eruption of the Bishop Tuff (Hildreth, 2004). Since that time, numerous smaller eruptions have occurred in the caldera and surroundings. In more recent times, caldera unrest has manifest in the form of earthquake swarms and episodic uplift of caldera's central resurgent dome (Hill, 2006; Hill et al., 2003; Hill and Prejean, 2005; Montgomery-Brown et al., 2015), with major episodes of seismicity and uplift in 1980 and 1997. These uplift sequences are thought to be caused by intrusion of magma into bodies at depths of 4 to 10 km beneath the resurgent dome (Hill, 1992). The ~5-month-long 2014 earthquake swarm was the largest observed in the caldera since 1997, with more than 3300 events cataloged by the Northern California Seismic Network (NCSN), including three of moment magnitude $M_w = 3.5$. A map of our study area, including historic seismicity and the 2014 swarm, is shown in Fig. 1.

Earthquake swarms are common in volcanic and hydrothermal settings (Hill, 1977; Sibson, 1987; Fischer et al., 2014; Zaliapin and Ben-Zion, 2013) and are sometimes attributed to transient fluid pressure changes within a network of near-critically stressed fractures or faults (Hainzl et al., 2004; Schoenball and Ellsworth, 2017; Shelly et al., 2013). The high quality seismic network that recorded the 2014 Long Valley Caldera swarm provides data at a resolution necessary to investigate the processes involved in swarm activation. In particular, high-precision earthquake relocations and a large number of focal mechanism solutions allow for interpretation of the fault network geometry and the evolution of the stimulated region in greater detail.

Shelly et al. (2016b) demonstrated a systematic mismatch between the overall trend in the migration patterns and the fault plane geometry inferred from the focal mechanism solutions. One possible mechanism that could account for this contradictory observation is that a set of en-echelon faults that hosted the seismic events were connected by dilational joints. The faults would tend to be in a near-critical stress orientation, and the dilational joints would necessarily be oriented in the plane perpendicular to the least principal stress. This type of mixed-mechanism fracturing process has been interpreted to have occurred during hydraulic stimulation treatments at the Fenton Hill enhanced geothermal system test site (Norbeck et al., 2018). It is possible that mixed-mechanism fracturing, in which fluid-faulting interactions are controlled by a mixture of sliding-mode and opening-mode fracture deformation, occurs commonly in igneous rock settings (Hill, 1977; Sibson, 1987). A more thorough understanding of mixed-mechanism behavior would help to inform hazard for both natural geologic earthquake swarms as well as cases of injection-induced seismicity. In this study, we used a numerical model to investigate the 2014 Long Valley Caldera earthquake sequence and determine whether mixed-mechanism fracturing could plausibly explain behavior observed during the swarm.

2. FAULT NETWORK STRUCTURE REVEALED THROUGH SEISMICITY AND FOCAL MECHANISMS

The 2014 Long Valley swarm has been the subject of extensive seismological analyses aimed at illuminating the faulted structure. Shelly et al., (2016a) used 3312 routinely cataloged earthquakes to detect a total of 8494 events that could be precisely relocated between May 31 and November 1, 2014. All events were relocated simultaneously using hypoDD (Waldhauser and Ellsworth, 2000), constrained by 39 million correlation-derived differential times. Based on this analysis, including the spatial-temporal progression of seismicity, the authors proposed that the swarm was caused by interactions between elevated fluid pressure and faulting.

To gain further insight into the structure and mechanics of faulting Shelly et al., (2016b) developed a technique to derive focal mechanisms for large populations of the swarm events, using correlation-derived relative polarities and cluster analysis. The fault plane orientation suggested by the focal mechanisms (see Fig. 2a) largely agreed with the structure as defined by seismicity, providing an additional means for grouping events on common structures. This analysis supported the earlier interpretation the swarm occurred along several fault structures, with increasing complexity in shallower, later stage of the swarm. The focal mechanism analysis also revealed new features. These included areas of faulting complexity (perhaps conjugate faulting) in areas where such structures were not apparent even in high-precision locations. In addition, a small but persistent mismatch was identified between the alignments of seismicity and the faulting orientations. Shelly et al. (2016b) proposed that this mismatch could plausibly be explained by linked shear and dilational fault structures (see Fig. 2b) as sometimes observed in geological outcrop (Sibson, 1996).

3. STRESS TENSOR INVERSION

Earthquake focal mechanism solutions describe the geometry of the fault plane on which slip occurred as well as the orientation of the slip vector. Groups of focal mechanism solutions contain information that can be used to constrain the state of stress in the subsurface. Methods have been developed to invert for the best-fitting principal stress orientations and relative stress magnitudes given a set of focal mechanism solutions in relatively close proximity (Hardebeck and Michael, 2006; Martínez-Garzón et al., 2014; Michael, 1984; Michael, 1987). These methods are based on the assumption that the maximum resolved shear traction on a given fault should be parallel to the slip vector from the focal mechanism solution. This type of stress inversion technique has been applied successfully in a variety of tectonic settings, including southern California (Hardebeck and Hauksson, 2001; Hardebeck and Michael, 2006), the New Madrid Seismic Zone (Hurd and Zoback, 2012), north-central Oklahoma (Walsh and Zoback, 2016), and The Geysers geothermal field in northern California (Martínez-Garzón et al., 2014).

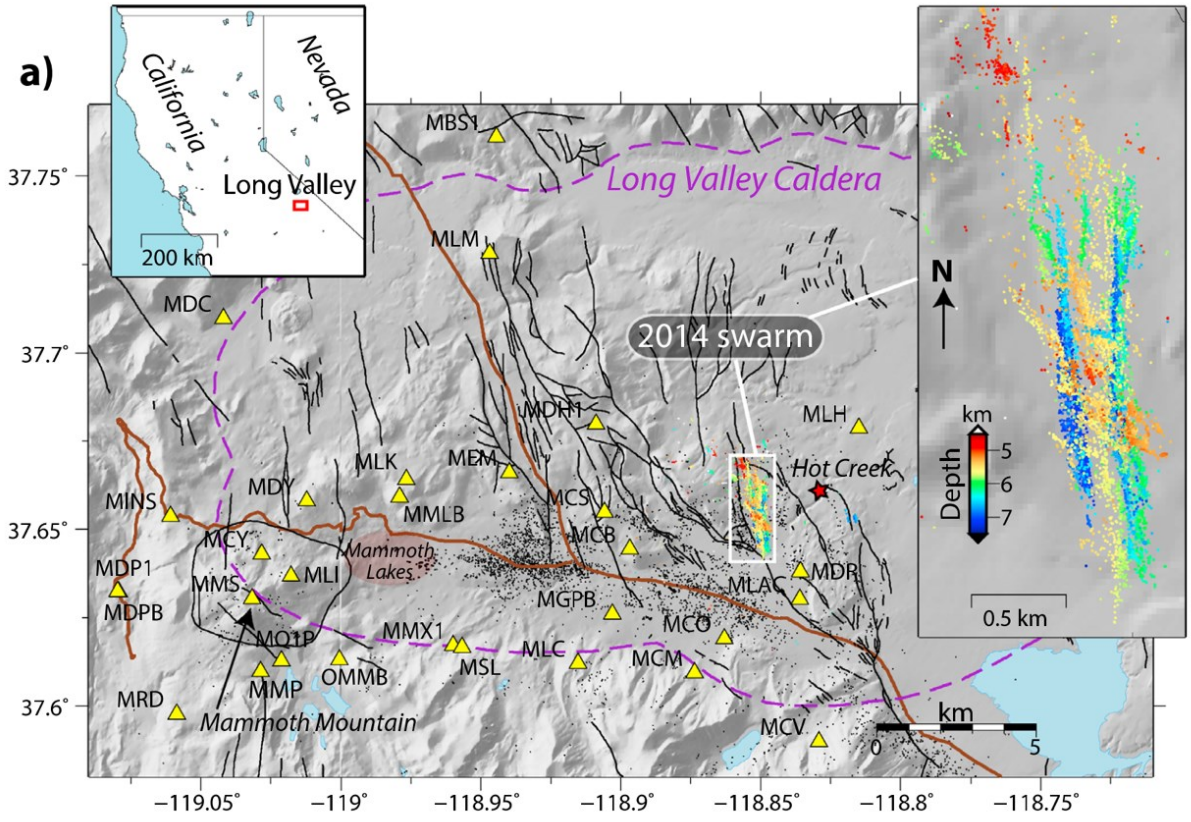

Figure 1. Map illustrating the Long Valley Caldera study area. Colored dots show relocated earthquake locations during the 2014 swarm (colored by depth). Black dots show relocated seismicity between 1984 to 2011. Purple dashed line shows the boundary of the caldera. Yellow triangles show seismic stations. Figure modified from Shelly et al. (2016a).

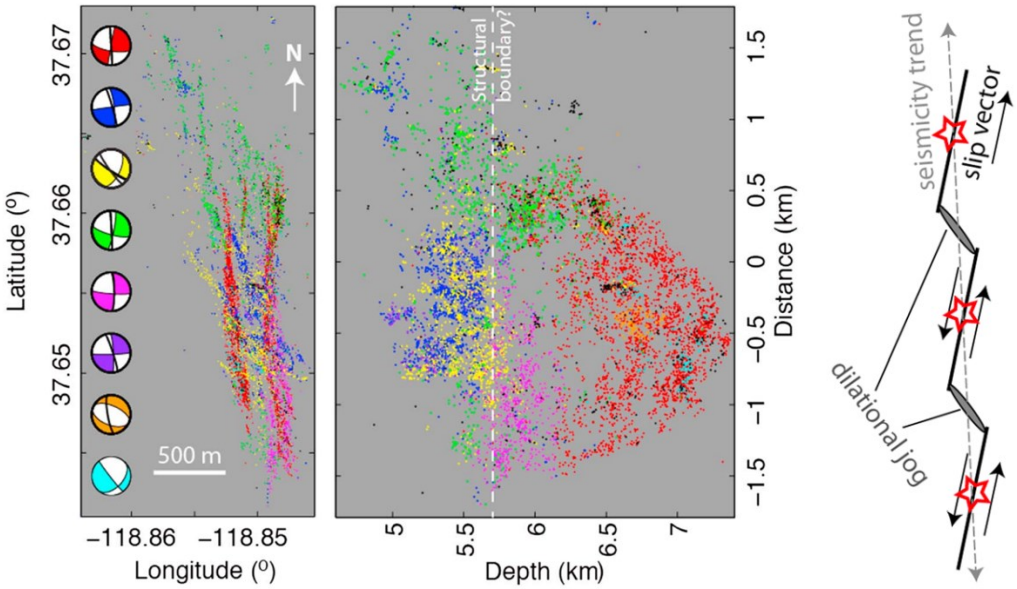

a) b)

Figure 2. a) Distribution of seismicity during the 2014 Long Valley Caldera earthquake swarm. Events are colored according to one of eight different focal mechanism solutions. The dark lines on the focal mechanism solutions represent the average trend of the seismicity. b) Schematic of the mixed-mechanism fracturing conceptual model. A series of en-echelon fractures well-oriented for slip in the current stress field are linked together by dilational jogs that are oriented in the plane perpendicular to the minimum principal stress. The red stars indicate the locations of seismic events that would be recorded. The dilational jogs could be preexisting or newly formed fractures propagating as hydraulic splay fractures. Figures modified from Shelly et al. (2016b).

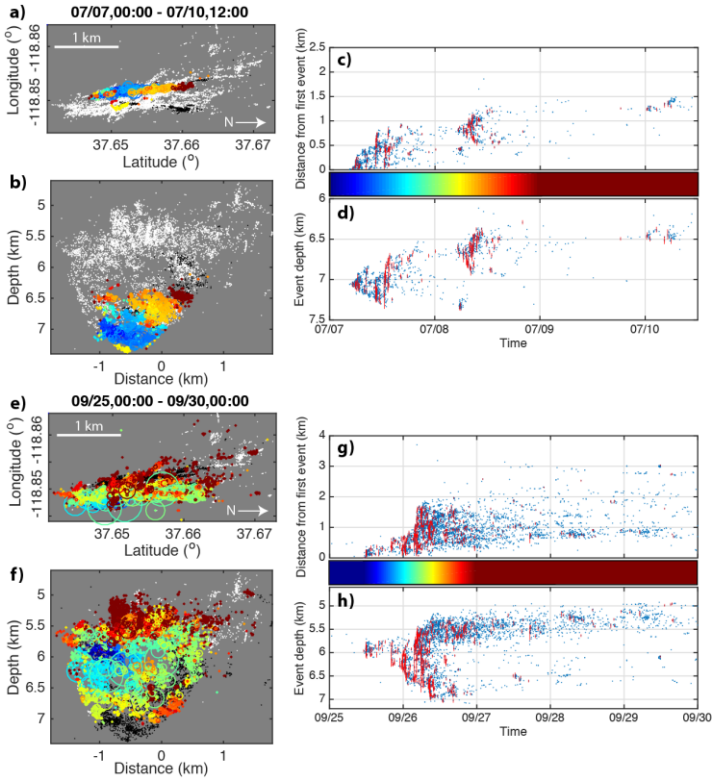

Figure 3. Observed spatial-temporal progression of seismicity for two major swarms in the 2014 Long Valley Caldera sequence. Events are colored by timing and the circle size is scaled by magnitude. The vertical red lines in (c), (d), (g), and (h) represent the approximate source dimensions for events with $M_w > 1$. Figure modified from Shelly et al. (2016a).

We used the MSATSI software developed by Martínez-Garzón et al. (2014) to invert for the state of stress at the Long Valley Caldera using the set of focal mechanism solutions that were compiled originally by Shelly et al. (2016b) (described in Sect. 2). The inputs to the algorithm are the set of fault planes and slip vectors associated with each focal mechanism. Shelly et al. (2016b) associated each of the 8494 earthquakes in the catalog with one of 20 different focal mechanism solutions. The stress inversion is sensitive to the relative number of focal mechanism solutions, so we used this full catalog of focal mechanisms in our inversion. Each focal mechanism provides two orthogonal fault planes that are equally valid, therefore the user is allowed to specify whether a particular plane is preferred. We assumed that the preferred plane was the plane that was most similar to the overall trend of the seismicity for each of the 20 clusters. We tested the sensitivity of using both the preferred plane and the auxiliary plane as inputs to the inversion. The algorithm provided the best-fit solution for the stress orientations and relative stress magnitudes. A bootstrap resampling technique was then used to estimate confidence intervals in the best-fit solution. We varied the number of resamples between 500 and 2000 and found that the solutions were not sensitive to the level of resampling. Finally, we performed the stress inversion using focal mechanisms based on each of the four focal mechanism calculation techniques described by Shelly et al. (2016b).

The results of the stress inversion are shown in Fig. 4. Each panel shows a stereonet that describes the orientation of the three principal stresses. The best-fitting solutions are shown as open circles, and the uncertainty range is illustrated as the colored circles. The orientation of the minimum principal stress is fairly well constrained to be slightly subhorizontal at an azimuth ranging between 225° to 245°. The orientations of the intermediate and maximum principal stresses exhibit more variability. Given that the set of focal mechanism solutions contains both strike-slip and normal faulting events, it is likely that the intermediate and maximum principal stress magnitudes are similar. In the stress inversion, this ambiguity can appear as an overlap in the confidence intervals of the intermediate and maximum principal stress orientations. We see evidence for this behavior, for example, in the inversions based on the catalog composite set of mechanisms (left column in Fig. 4). The majority of the inversions suggest that the intermediate principal stress is near vertical and the maximum principal stress is subhorizontal.

The stress inversions provide the parameters R and ϕ which define the relative magnitudes of the principal stresses (Martínez-Garzón et al., 2014):

$$\phi = 1 - R = \frac{\sigma_2 - \sigma_3}{\sigma_1 - \sigma_3}, \tag{1}$$

where σ_1, σ_2, and σ_3 are the maximum, intermediate, and minimum principal stress magnitudes, respectively. Note that this analysis must be performed in effective stress space. Equation 1 alone does not provide enough information to constrain all of the stress magnitudes. Based on the theory of the critically-stressed crust, frictional equilibrium provides an additional constraint on the relative stress magnitudes (Zoback, 2007):

$$\frac{\sigma_1}{\sigma_3} \leq k, \tag{2}$$

where k depends on the friction coefficient, f, and is defined as:

$$k = \left[(f^2 + 1)^{1/2} + f\right]^2. \tag{3}$$

Assuming that the friction coefficient can be estimated, Eqs. 1 and 2 provide two equations for the three unknown magnitudes of the principal stresses. A third constraint can be determined if there is knowledge of the magnitude of the vertical stress. The stress inversions for the Long Valley area suggest that the principal coordinate system is not exactly aligned in the horizontal and vertical directions. For the general case, the state of stress in a rotated coordinate system is:

$$\boldsymbol{\sigma}' = \mathbf{M}\boldsymbol{\sigma}\mathbf{M}^T, \tag{4}$$

where $\boldsymbol{\sigma}$ is the stress tensor in the original coordinate system, $\boldsymbol{\sigma}'$ is the stress tensor in the new coordinate system, and $\mathbf{M}$ is the transformation matrix of direction cosines that relate the two coordinate systems. Taking $\boldsymbol{\sigma}$ to represent the stress tensor in the horizontal/vertical coordinate system, the vertical normal stress component is related to the three principal stresses through the following relationship:

$$\sigma_V = \sigma_{z'z'} = m_{xz'}^2\sigma_1 + m_{yz'}^2\sigma_2 + m_{zz'}^2\sigma_3 = l^2\sigma_1 + m^2\sigma_2 + n^2\sigma_3. \tag{5}$$

The magnitudes of the three principal stresses can be found by combining Eqs. 1, 2, and 5. For example, we can first calculate σ_3 and then back-calculate the other stresses:

$$\sigma_3 = \frac{\sigma_V}{l^2 k + m^2(\phi k - \phi + 1) + n^2}, \tag{6}$$

$$\sigma_2 = (\phi k - \phi + 1)\sigma_3, \tag{7}$$

$$\sigma_1 = k\sigma_3. \tag{8}$$

The principal stresses at Long Valley are not oriented exactly in the vertical/horizontal directions, but for the purposes of our study it is sufficient to approximate them as such. To estimate the stress magnitudes at depth, we assumed that the vertical stress is the intermediate principal stress (based on the mixture of both strike-slip and normal faulting focal mechanisms shown in Fig. 2a). The vertical stress and ambient fluid pressure gradients were assumed to be $\sigma_V = 25$ MPa/km and $p = 10$ MPa/km. The best-fit values of the stress ratio parameter obtained from the suite of inversions ranged from $0.38 \leq \phi \leq 0.91$. Taking a nominal value for the friction coefficient of $f = 0.6$ yields $k = 3.1$. Using the methodology described above, the magnitude of the minimum and maximum principal stresses were estimated to range from $15.1 \leq \sigma_3 \leq 18.3$ MPa/km and $26.0 \leq \sigma_1 \leq 36.0$ MPa/km, respectively. Under the assumption that the in-situ stresses developed over geologic time in response to fault friction equilibrium, our stress magnitude estimates should be interpreted as bounding limits on the state of stress.

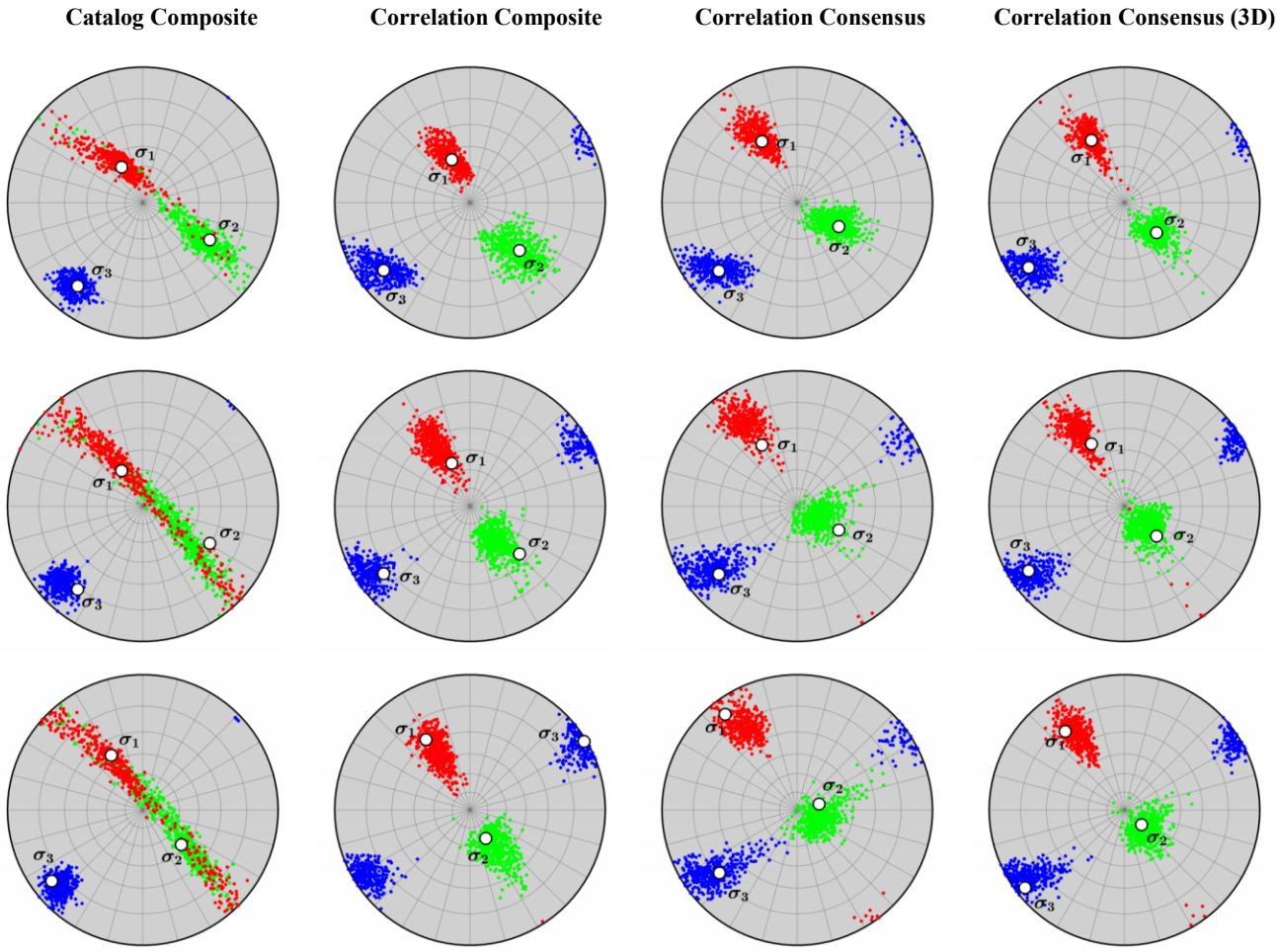

Figure 4. Stereonets showing the orientation of the principal stress tensor resulting from the stress inversion. Each of the columns represent the stress inversion results obtained by using the focal mechanism catalogs that were calculated using the four techniques described by Shelly et al. (2016b). The rows illustrate the sensitivity of the stress inversion to the focal mechanism plane selected for the algorithm; algorithm not informed of preferred plane (top row), auxiliary plane selected as preferred plane (middle row), fault plane inferred from trend in seismicity selected as preferred plane (bottom row).

4. HYDROMECHANICAL MODELING OF THE LONG VALLEY CALDERA EARTHQUAKE SWARM

We performed hydromechanical modeling to investigate the potential influence of mixed-mechanism fracturing in controlling the overall migration patterns during the 2014 earthquake swarm at Long Valley Caldera, California. The numerical simulations were performed using the CFRAC reservoir simulation software (McClure and Horne, 2013; McClure et al., 2016; Norbeck, 2016; Norbeck et al., 2016). The CFRAC reservoir simulator calculates the coupled interaction between fluid flow and mechanical deformation in three-dimensional discrete fracture networks (McClure et al., 2016). Fracture sliding deformation was evaluated using a static/dynamic treatment for friction. We considered the nucleation and propagation of tensile fractures that splay from the tips of natural fractures. In Sects. 4.1 through 4.4, we review the mathematical formulation for the various components of the numerical model. In Sect. 4.5, we present our geomechanical and structural conceptual model for the Long Valley Caldera hydrothermal area.

4.1 Coupled fluid flow and fracture deformation

In the model, fluid flow occurs through a network of preexisting natural fractures as well as newly formed hydraulic splay fractures. Each fracture can transmit and store fluids, and their hydraulic properties can be influenced by the local state of stress and shear deformation. Fluid flow in the rock surrounding the fractures are neglected under the assumption of extremely low permeability of granite, therefore flow only occurs in the fractures. The fractures are assumed to be fully saturated with a single phase, slightly compressible fluid. Isothermal conditions are assumed. Mass balance for flow in the fractures can be expressed as:

$$\nabla \cdot \left(\frac{\rho}{\mu} T \nabla p\right) + \widetilde{m} = \frac{\partial}{\partial t}(\rho E), \tag{9}$$

where ρ is fluid density, μ is fluid viscosity, p is fluid pressure, T is fracture transmissivity, $E$is fracture void aperture, and $\widetilde{m}$ is a fluid mass source term. The fracture transmissivity is assumed to behave according to the cubic law for flow through parallel fracture surfaces (Witherspoon et al., 1980):

$$T = \frac{e^3}{12}, \tag{10}$$

where e is fracture hydraulic aperture. The fluid density is calculated as $\rho = \rho_* exp[c_w(p - p_*)]$, where ρ_* is a reference density, c_w is water compressibility, and p_* is a reference fluid pressure. Fluid viscosity is constant.

To perform the fracture opening and sliding calculations, mechanical equilibrium is enforced in both the mode-I and mode-II directions. If the fluid pressure in a fracture exceeds its normal stress the fracture will begin to open as the fracture walls separate. The opening-mode deformation will induce stress changes that act to balance the fluid overpressure, therefore mode-I mechanical equilibrium can be described as:

$$\sigma_{n0} + \Delta\sigma_n - p \equiv 0, \tag{11}$$

where σ_{n0} is the normal stress resolved on the fracture due to the remote loading conditions and $\Delta\sigma_n$ is the change in normal stress caused by fracture deformation. If the shear strength of the fracture exceeds the shear stress acting on the fracture, the fracture is assumed to be locked. Once the shear stress becomes equal to the shear strength sliding begins to occur and mode-II mechanical equilibrium can be described as:

$$\tau_0 + \Delta\tau - \eta V \equiv f(\sigma_n - p) + s, \tag{12}$$

where τ_0 is the shear stress resolved on the fracture due to remote loading conditions, $\Delta\tau$ is the change in shear stress caused by fracture deformation, η is the inertial damping parameter, V is the sliding velocity along the fracture, f is friction coefficient, $\sigma_n - p$ is the effective normal stress acting on the fracture, and s is fracture cohesion. In Eq. 12, the terms on the left-hand side represent the driving stress acting to encourage sliding $(\tau = \tau_0 + \Delta\tau - \eta V)$, and the terms on the right-hand side represent the frictional resistance to slip $(\tau_r = f(\sigma_n - p) + s)$. In this work, we use a static/dynamic treatment for fault friction evolution (described in detail in Sect. 4.3). The sliding velocity is defined as the instantaneous rate of change of shear displacement, δ:

$$V = \frac{d\delta}{dt}. \tag{13}$$

In Eq. 12, the term ηV is an approximation for the dynamic stress drop caused by radiated energy while slip is occurring at relatively high slip speeds (Segall, 2010), and also has the advantageous numerical property of setting a limit on how rapidly sliding can occur, which is especially important when effective stress is near zero.

The faults and fractures are discretized into discrete elements. The numerical methods we use do not require discretization of the rock surrounding the fractures. The fluid mass balance equation (see Eq. 9) is solved using a discrete fracture model finite volume approach (Karimi-Fard et al., 2004). The mechanical boundary conditions (see Eqs. 11 and 12) are enforced by using a displacement discontinuity boundary element method to relate changes in stress to fracture deformation as:

$$\begin{Bmatrix} \mathbf{\Delta\tau} \\ \mathbf{\Delta\sigma_n} \end{Bmatrix} = \mathbf{A} \begin{Bmatrix} \mathbf{\Delta\delta} \\ \mathbf{\Delta e} \end{Bmatrix} \tag{14}$$

where $\mathbf{A}$ is the matrix of stress-displacement Green's function solutions for fault deformation in a three-dimensional half-space (Okada, 1992), $\mathbf{\Delta\tau}$ and $\mathbf{\Delta\sigma_n}$ are vectors of the traction boundary conditions, and $\mathbf{\Delta\delta}$ and $\mathbf{\Delta e}$ are vectors of the displacement discontinuities. The hierarchical matrix approximation algorithm described by Bradley (2014) is used to perform the stress-displacement matrix-vector products efficiently. The fluid flow and fracture deformation calculations are performed using a sequential coupling strategy (McClure and Horne, 2013; Chapter 2 in Norbeck, 2016).

4.2 Stress- and slip-dependent hydraulic properties

Both the hydraulic and void apertures can be influenced by deformation in the normal (mode-I) and sliding (mode-II) directions. When a fracture bears a compressive normal stress (i.e., $\sigma_n - p > 0$) the fracture aperture is calculated explicitly according to a nonlinear joint stiffness relationship (Willis-Richards et al., 1996):

$$e(\sigma_n, p, \delta) = \frac{e_*}{1+9\left(\frac{\sigma_n - p}{\sigma_{*e}}\right)} + \delta \tan\left(\frac{\varphi}{1+9\left(\frac{\sigma_n - p}{\sigma_{*e}}\right)}\right) + e_{res}. \tag{15}$$

In Eq. 15, e_* and σ_* are constants that define the normal stiffness, δ is cumulative shear slip, φ is shear dilation angle, and e_{res} is the residual fracture aperture. The first term on the right-hand side controls the influence of opening-mode deformations, and the second term is related to shear-enhanced dilation as fractures slide. If the fluid pressure overcomes the normal stress acting on the fracture (i.e., $\sigma_n - p < 0$) then the opening-mode deformation is calculated according to fracture mechanics using a boundary element method, and the fracture aperture is calculated as:

$$e(\sigma_n, p, \delta) = e_* + \Delta e + \delta \tan\varphi_e \ + e_{res}, \tag{16}$$

where Δe is the opening-mode fracture deformation. Equations 15 and 16 are continuous as the fracture transitions from "closed" to "open." A similar set of equations is used for void aperture, E, where the constants are allowed to be different. The variability of hydraulic properties with stress and slip can cause Eq. 9 to evolve in a highly nonlinear fashion.

4.3 Earthquake ruptures with static/dynamic friction evolution

To perform the sliding deformation calculations, we use a static/dynamic treatment to evaluate the fracture friction coefficient. When the fracture is stuck the friction coefficient is evaluated as the static value, f_S. Once the frictional strength is met or exceeded, the friction coefficient is dropped instantaneously to a lower dynamic value, f_D. This treatment can be described as:

$$f = \begin{cases} f_S, & \text{if } |\tau| > f_S(\sigma_n - p) + s, \\ f_D, & \text{if } |\tau| \leq f_S(\sigma_n - p) + s. \end{cases} \tag{17}$$

We use a relatively ad-hoc method to restrengthen the friction coefficient once 80% of the stress drop has occurred (McClure, 2015):

$$|\tau| < [f_D + 0.2(f_S - f_D)](\sigma_n - p) + s. \tag{18}$$

While the static/dynamic treatment has some limitations and is subject to discretization-dependence, it provides a useful and efficient means to simulate earthquake ruptures given that slip on one fracture element can transfer stress to nearby elements leading to cascading rupture (Baisch et al., 2010; McClure, 2015).

The evolution of sliding velocity can be used to determine whether slip occurs as a seismic event or as a slow-slip event. Once sliding velocity exceeds a threshold value and earthquake rupture event is activated and the slip accumulated during the event can be integrated over the slipping patch of the fault to calculate the earthquake moment magnitude. Eventually, the earthquake rupture arrests and the sliding velocity reduces to low values signaling the end of the earthquake rupture. The seismic moment release is calculated as:

$$M_0 = G \int_A \ \Delta\delta \ dA, \tag{19}$$

where G is the shear modulus of rock, $\Delta\delta$ is the shear slip accumulated during the earthquake rupture, and A is the surface area of the fault patch that ruptured. Seismic moment can then be used to calculate the moment magnitude. In this work, we consider an earthquake rupture to have nucleated once the sliding velocity increases above the threshold value of 5×10^{-3} m/s. The fault element that first exceeds this criterion is used to define the hypocentral location of the seismic event.

4.4 Propagation of hydraulic splay fractures

The mixed-mechanism conceptual model relies on the interaction between preexisting natural fractures and propagating hydraulic fractures. The numerical method used to perform the fracture propagation calculations has been described by McClure (2015). A set of potentially forming hydraulic fractures are specified stochastically at the beginning of a simulation. The state of stress is continually evaluated for all fracture elements, and if the fluid pressure of a potentially forming crack-tip element reaches the least principal stress the

element is activated. Once an element becomes active, the mode-I stress intensity factor is calculated using an approach developed for the displacement discontinuity method (Norbeck et al., 2016; Olson, 2007):

$$K_I = 0.806\left(\frac{Y}{4(1-\nu^2)}\right)\left(\frac{\pi}{a}\right)^{1/2}\Delta e, \tag{20}$$

where Y is Young's modulus, ν is Poisson's ratio, a is the half-length of the crack-tip element, and Δe is the mode-I displacement discontinuity of the crack-tip element. Once K_I exceeds the mode-I fracture toughness, K_{Ic}, the element is allowed to "nucleate," and the element is added into the fluid flow and fracture mechanics systems of equations. The splay fractures are assumed to propagate in the plane perpendicular to the least principal stress. We use an ad-hoc criterion to determine whether the hydraulic fractures are able to propagate through or terminate against a natural fracture. We simply prescribe a termination frequency, and whenever a hydraulic fracture intersects a natural fracture a random draw is performed to determine whether or not to arrest the hydrofrac (Norbeck et al., 2018). In this work, we tested a range of termination frequencies to evaluate its impact on the overall migration pattern of the seismic swarm.

4.5 Geomechanical and structural conceptual model for the Long Valley Caldera hydrothermal area

The results of the stress tensor inversion were integrated with the fault structure characterization to develop a conceptual model of the Long Valley Caldera hydrothermal system. A detailed three-dimensional discrete fracture network model was then generated to perform the CFRAC hydromechanical simulations. Here we discuss the important assumptions that were made in the course of developing the reservoir model. Lists of the model properties are provided in Tables 1 through 3.

The fractured reservoir was centered at a depth of 6 km. The principal stress tensor was assumed to be oriented in the vertical and horizontal directions. The stress gradients were specified as: $d\sigma_V/dz = 25$ MPa/km, $d\sigma_H/dz = 27$ MPa/km, and $d\sigma_h/dz = 16$ MPa/km. Therefore, at the reservoir depth the principal stresses were: $\sigma_V = 150$ MPa, $\sigma_H = 162$ MPa, and $\sigma_h = 96$ MPa. The mean normal stress at the reservoir depth was $\sigma_m = (\sigma_V + \sigma_H + \sigma_h)/3 = 136$ MPa. Fluid pressure was assumed to be hydrostatic ($dp/dz = 10$ MPa/km) corresponding to an initial reservoir pressure of $p_0 = 60$ MPa. The maximum and minimum principal stresses were oriented at azimuths of α_{σ_H} =N150°E and α_{σ_h} =N240°E, respectively. The state of stress at 6 km depth is illustrated graphically in Fig. 5.

We identified two predominant natural fracture sets based on the focal mechanism categories presented by Shelly et al. (2016b). The primary fracture set (F1) and secondary fracture set (F2) were oriented at azimuths of α_{F1} =N7°E and α_{F2} =N127°E. Each of these fracture sets are near-critically stressed in the present-day stress field (see Fig. 5). The fracture sets strike roughly 60° apart, suggesting that the fractures may have formed contemporaneously as conjugate fracture sets before the stress tensor realigned to its present condition. To generate the three-dimensional discrete fracture network, natural fractures were specified stochastically with average orientations equal to the azimuths α_{F1} and α_{F2}. The number of fractures in each set was based loosely on the relative number of seismic events associated with the two focal mechanisms (the primary fracture set F1 made up 75% of the total number of fractures). A set of "potentially forming" hydraulic fractures were specified in the orientation of the maximum horizontal stress (i.e., in the plane perpendicular to the minimum horizontal stress). The potentially forming fractures represented splay fractures that were able to nucleate off the tips of the preexisting fractures and propagate as fluid-driven hydraulic fractures.

A primary focus of this study was to investigate how a potential fluid source may have initiated the seismic swarm and the extent to which that source may have controlled the overall migration of seismicity. Determining constraints on the properties of the fluid source (e.g., the total fluid volume and duration) will have important consequences for evaluating the hazard related to earthquake sequences in active hydrothermal regions. In the context of the mixed-mechanism fracturing hypothesis, the fluid pressure from the active source must have been near or greater than the magnitude of the least principal stress to encourage the formation of new tensile fractures. Is there a mechanism that would allow for a sustained, high-pressure fluid source at seismogenic depths?

In the brittle regime of the upper crust, fluid pressure typically equilibrates to hydrostatic values. The principal earth stresses evolve in concert with this level of fluid pressure as faulting occurs (Townend and Zoback, 2000). An upper-bound on fluid pressure is set by the magnitude of the minimum principal stress because hydraulic fractures are able to form once that level of fluid pressure is reached. However, in the ductile regime of the upper crust it may be possible that lenses of fluid can become equilibrated with the lithostatic stresses if brittle fracturing and faulting play less of a role in controlling the state of stress. At the Long Valley Caldera, the brittle-ductile transition is estimated to exist at approximately 6 to 8 km depth based on the lower limit of seismicity observed since 1984 (Hill, 1992). The deepest events in the 2014 swarm are consistent with the interpretation that the brittle-ductile transition at Long Valley Caldera exists at approximately 8 km depth. We propose that just below the fractured reservoir, fluid pressure may have been elevated to values approaching the mean normal stress; flow from a highly pressurized region breached the brittle crust along a fault or along a newly formed tensile fracture, ultimately initiating the swarm.

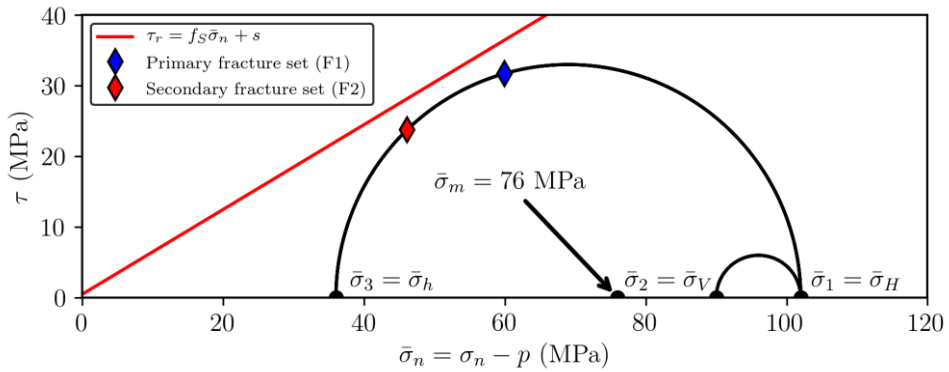

Figure 5. Mohr circle representation of the state of stress at 6 km depth near the Long Valley Caldera. The black circles represent the magnitudes of the three principal stresses and the mean normal stress. The colored diamonds represent the orientations of the primary (F1) and secondary (F2) fracture sets in the model. The red line represents the shear failure envelope.

5. RESULTS

We simulated a four-day period to represent similar time frames as the two most intense periods of swarm activity (see Fig. 3). An overpressured fluid source located near the bottom of the model domain injected water at a constant rate of 400 kg/s. An upper bound on the injection pressure was set equal to the mean normal stress at 6 km depth. The location, timing, and magnitude of individual earthquake events were tracked throughout the simulation.

We found that the mixed-mechanism fracturing hypothesis can reasonably reproduce the important characteristics of the swarm sequences. The evolution of the stimulated fracture network is shown in Figs. 6 and 7. As fluid migrated through the network of natural fractures, the fractures tended to slip at seismic slip speeds. Stress redistribution near the fracture tips caused tensile fractures to nucleate and propagate in the direction of maximum principal stress. The large fluid overpressure was sufficient to cause fracture propagation beyond the near-tip region that experienced the stress perturbations caused by slip on the natural fractures. The propagating hydraulic splay fractures sometimes terminated against neighboring natural fractures creating new hydraulic pathways that were able to accommodate the continual fluid source (see Fig. 6). Both natural fractures and newly formed tensile splay fractures contributed significantly to the fracture network activated during the swarm.

Plan and cross-sectional views of the distribution of seismicity are shown in Fig. 8. In plan view, the seismicity migrated in an overall north-south trend, despite the fact that the major slipping planes were oriented at N7°E. An example of a typical mixed-mechanism fracturing event is shown in Fig. 9. The hydraulic splay fractures connected multiple en-echelon fractures. It was necessary that the hydraulic splay fractures terminate against neighboring natural fractures (which was a model assumption) so that seismicity did not form broad trends in the direction of maximum principal stress. Seismicity tended to migrate to shallower depths over time (see Figs. 7, 8, and 10). The maximum recorded magnitude was slightly greater than $M_w = 3$ (see Fig. 10), which is consistent with the observed earthquake magnitudes during the 2014 Long Valley Caldera swarm. Bursts of seismic activity tended to occur as the splay fractures linked into new areas of natural fractures.

6. CONCLUSIONS

The 2014 Long Valley Caldera seismic swarm was the most productive sequence in the region since 1997 and included three magnitude 3.5 events. Previous studies have suggested that fluid migration through a network of critically-stress fractures and faults influenced the seismicity migration patterns (Shelly et al., 2016a,b). A particularly interesting observation was that the orientation in the overall trend in seismicity was systematically offset from the fault planes inferred from focal mechanism solutions (Shelly et al., 2016b). Other studies have interpreted similar observations during hydraulic stimulation experiments and attributed the behavior to a mixed-mechanism fracturing process (McClure and Horne, 2014; Norbeck et al., 2018).

We performed numerical simulations with a hydromechanical fractured reservoir model to investigate fluid-faulting interactions during the 2014 Long Valley Caldera swarm. The simulations were performed with a coupled fluid flow and fracture mechanics reservoir simulation software called CFRAC (McClure, 2012; Norbeck, 2016). Our simulations were consistent with the observed seismicity in that an overall north-south trend in seismicity occurred despite the ~N7˚E orientation of primary fracture set on which most of the earthquakes occurred. In the model, the mismatch in orientations was controlled by a combination of shear slip on the preexisting fractures and the formation and propagation of newly formed hydraulic splay fractures. Stress concentrations caused by shear slip on the natural fractures encouraged the splay fractures to nucleate. It was necessary that the propagating splay fractures terminate frequently against neighboring natural fractures to prevent dominant migrations patterns from forming in the direction of the maximum principal stress. Similar to the observations, seismicity in the model tended to migrate upward as the swarm progressed. Although this does not preclude other conceptual models, the broad agreement between the simulation results and the swarm behavior suggests it is plausible that mixed-mechanism fracturing played a dominant role in the evolution of the 2014 Long Valley Caldera sequence. The results of this study may have application to sequences of natural or induced seismicity in other hydrothermal settings with similar subsurface conditions and lithologies. Developing an improved understanding of the processes controlling behavior will help to inform seismic and volcanic hazard estimates in an active hydrothermal area.

Table 1. State of stress from stress tensor inversion.

Parameter	Value	Unit	Description
σ_V	150	MPa	Vertical stress at 6 km depth
σ_H	162	MPa	Maximum horizontal stress at 6 km depth
σ_h	96	MPa	Minimum horizontal stress at 6 km depth
p_0	60	MPa	Initial reservoir fluid pressure at 6 km depth
$d\sigma_V/dz$	25	MPa · km^{-1}	Vertical stress gradient
$d\sigma_H/dz$	27	MPa · km^{-1}	Maximum horizontal stress gradient
$d\sigma_h/dz$	16	MPa · km^{-1}	Minimum horizontal stress gradient
α_{σ_H}	N150°E	deg.	Azimuth of the maximum horizontal stress
α_{σ_h}	N240°E	deg.	Azimuth of the minimum horizontal stress
α_{F1}	N7°E	deg.	Azimuth of the primary fracture set
α_{F2}	N127°E	deg.	Azimuth of the secondary fracture set
D	6	km	Depth at the center of the model domain

Table 2. Fracture and rock properties.

Parameter	Value	Unit	Description
f_S	0.6	-	Static friction coefficient
f_D	0.55	-	Dynamic friction coefficient
s	0.5	MPa	Fracture cohesion
K_{Ic}	1.5	MPa · m$^{1/2}$	Mode-I fracture toughness
e_*	0.003	m	Reference fracture hydraulic aperture
E_*	0.0005	m	Reference fracture void aperture
e_{res}	0.000025	m	Residual hydraulic aperture
E_{res}	0.0001	m	Residual void aperture
σ_{*e}	25	MPa	Fracture normal stiffness parameter for hydraulic aperture
σ_{*E}	25	MPa	Fracture normal stiffness parameter for void aperture
φ_e	3	deg.	Shear dilation angle for hydraulic aperture
φ_E	1.5	deg.	Shear dilation angle for void aperture
G	30	GPa	Shear modulus of granite formation
ν	0.25	-	Poisson's ratio of granite formation
η	3.15	MPa · m^{-1} · s	Radiation damping parameter

Table 3. Fluid properties.

Parameter	Value	Unit	Description
μ	1.5×10^{-4}	Pa · s	Fluid viscosity
ρ_*	930	kg · m^{-3}	Reference fluid density
c_w	4.4×10^{-4}	MPa^{-1}	Water compressibility
p_*	0.14	MPa	Reference fluid pressure (atmospheric)

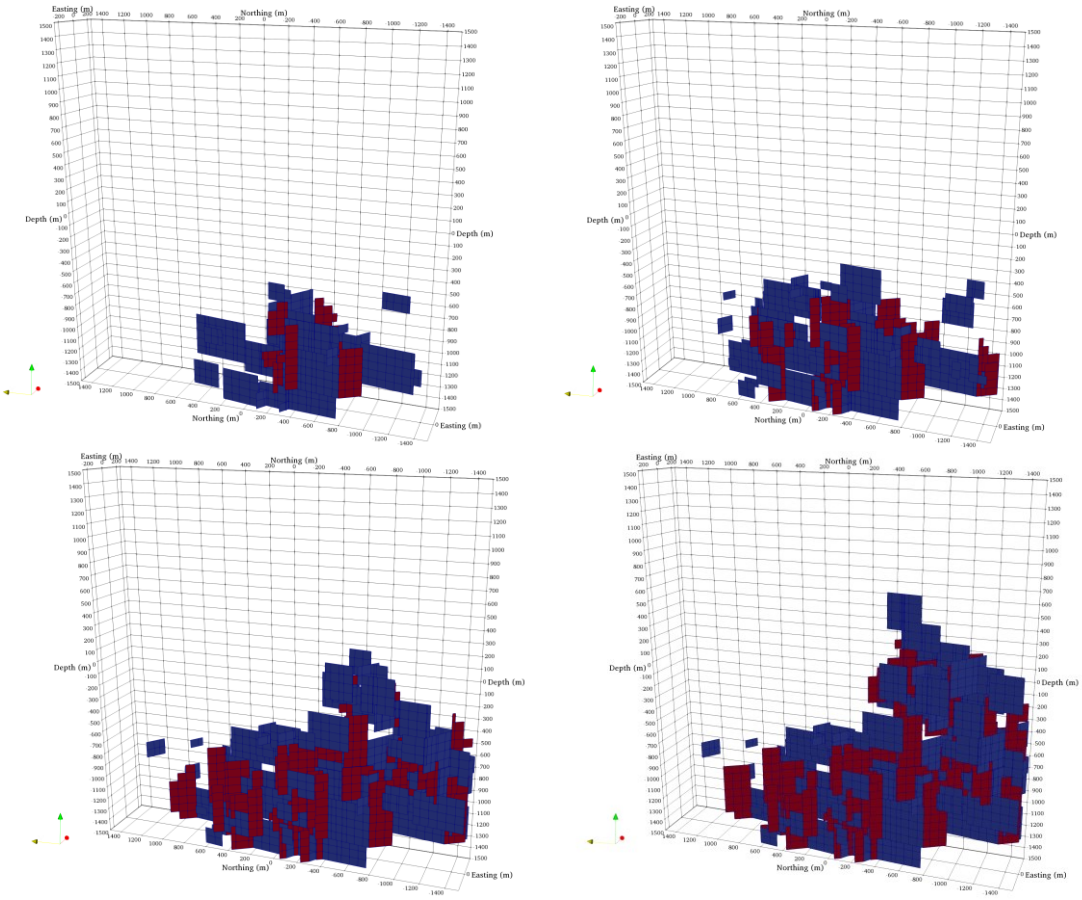

Figure 6. Distribution of preexisting natural fractures and newly formed hydraulic splay fractures throughout the evolution of the earthquake swarm. The blue fracture surfaces are preexisting fractures and the red fracture surfaces are newly formed mixed-mode splay fractures.

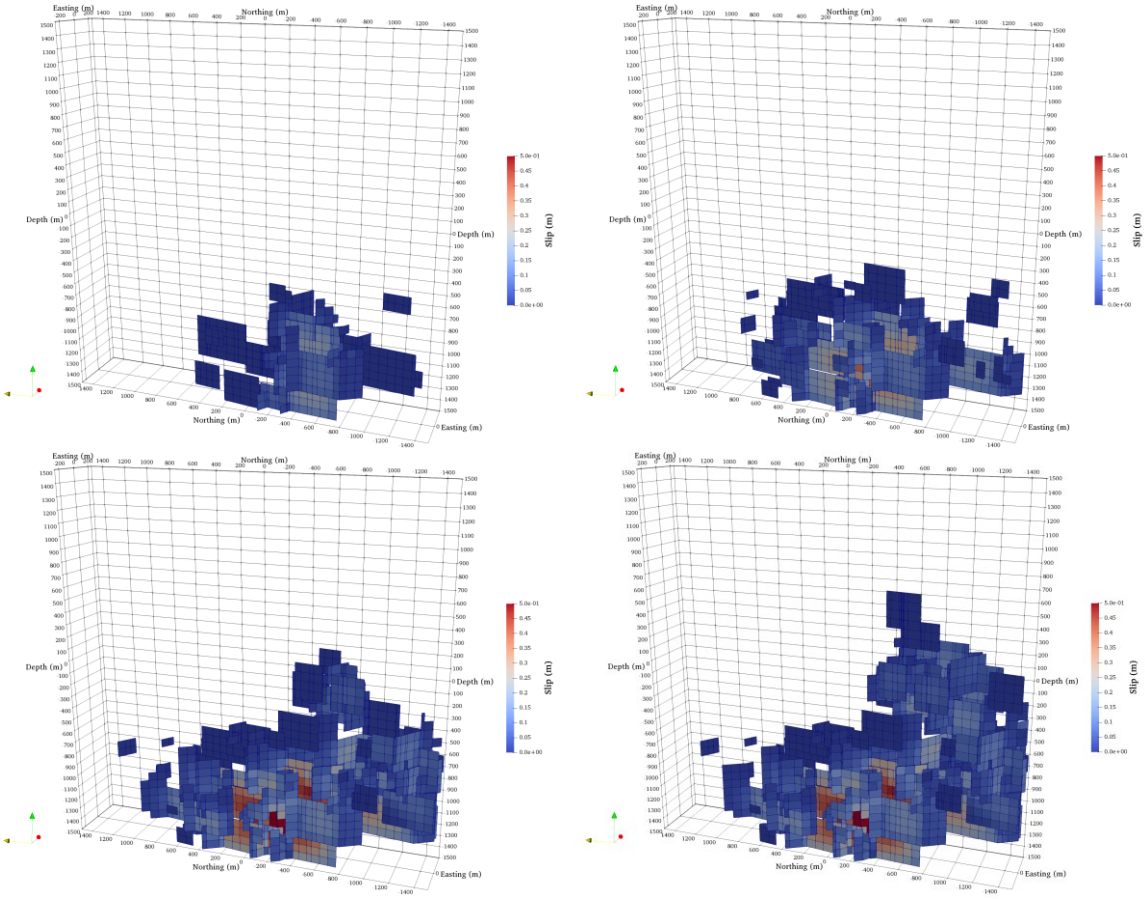

Figure 7. Evolution of the stimulated fracture network. Color scale represents the distribution of cumulative shear slip.

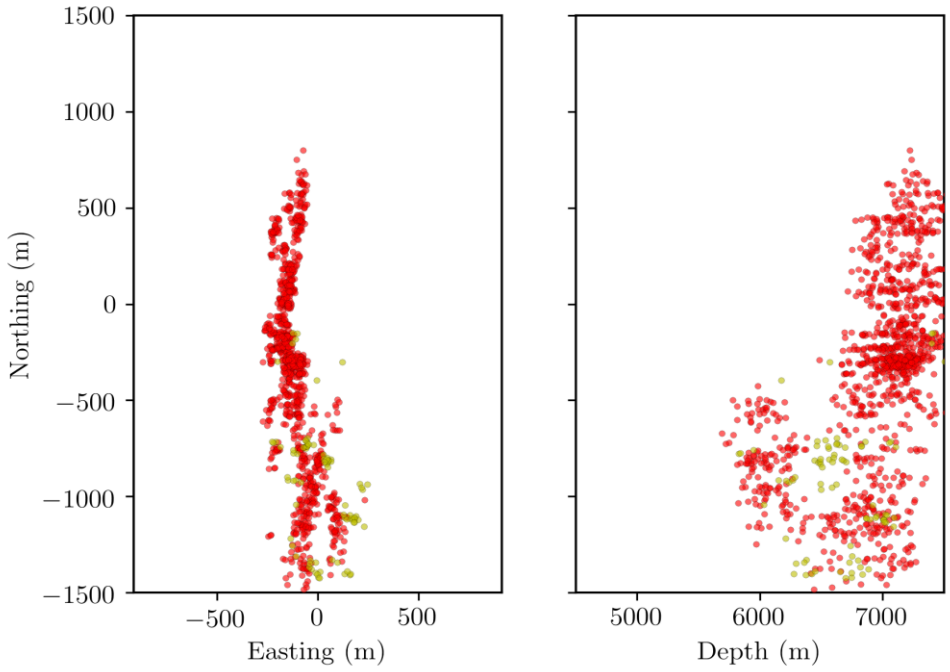

Figure 8. Distribution of modeled seismic events. The red and yellow dots represent the locations of earthquakes that occurred on F1 and F2 fractures, respectively.

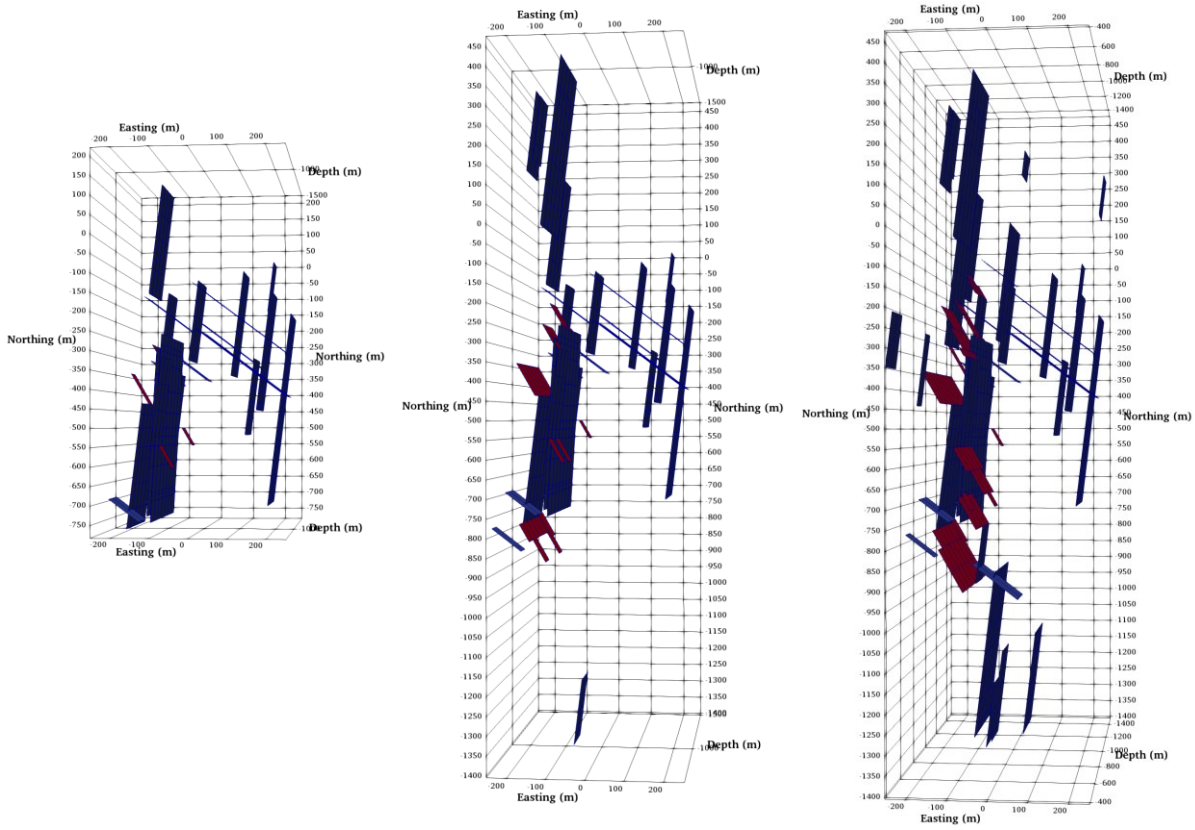

Figure 9. Illustration of the formation and propagation of splay fractures to create new hydraulic pathways between preexisting fractures. The blue fracture surfaces are preexisting fractures and the red fracture surfaces are newly formed mixed-mode splay fractures.

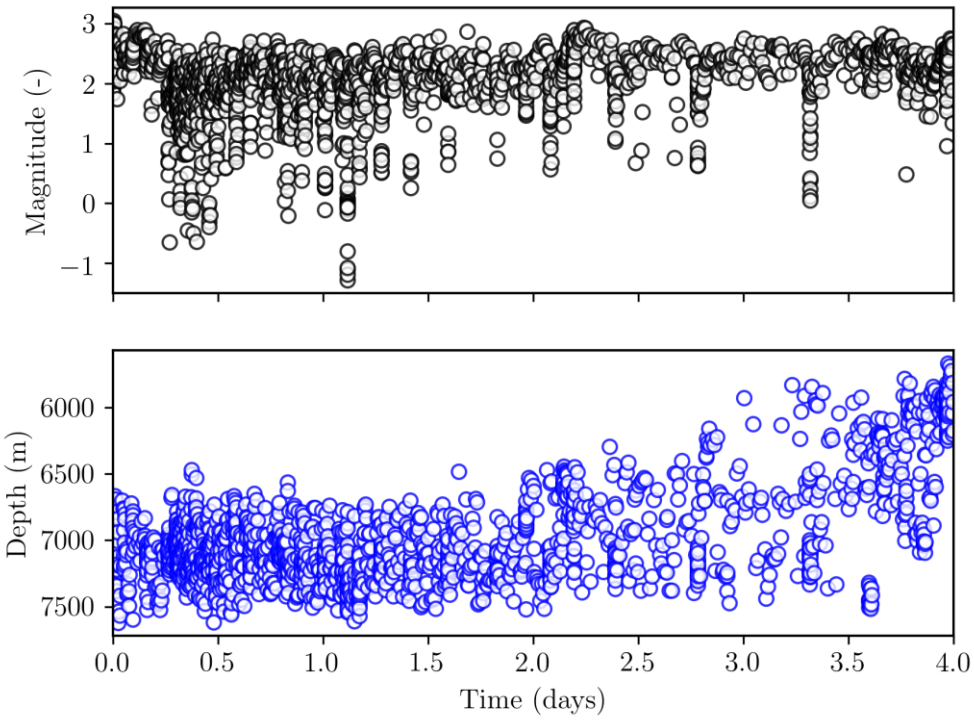

Figure 10. Earthquake magnitude (top) and event depth (bottom) over the duration of the four-day simulation period.

REFERENCES

Baisch, S., Vörös, R., Rothert, E. Stang, H., Jung, R., and Schellschmidt, R.: A numerical model for fluid injection induced seismicity at Soutz-sous-Forêts, *International Journal of Rock Mechanics & Mining Sciences*, **47**(3), (2010), 405-413, doi: 10.1016/j.ijrmms.2009.10.001.

Bradley, A.: Software for efficient static dislocation traction calculations in fault simulators, *Seismological Research Letters*, **85**(6), (2014), 1-8, doi: 10.1785/0220140092.

Fischer, T., Horálek, J., Hrubcová, P., Varycuk, V., Bräuer, K., and Kämpf, H.: Intra-continental earthquake swarms in West-Bohemia and Vogtland: A review, *Tectonophysics*, **611**, (2014), 1-27.

Hardebeck, J.L., and Hauksson, E.: Stress orientations obtained from earthquake focal mechanisms: What are appropriate uncertainty estimates?, *Bulletin of the Seismological Society of America*, **91**(2), (2001), 250-262, doi: 10.1785/0120000032.

Hardebeck, J.L., and Michael, A.J.: Damped regional-scale stress inversions: Methodology and examples for southern California and the Coalinga aftershock sequence, *Journal of Geophysical Research: Solid Earth*, **111**, (2006), B11310, doi: 10.1029/2005JB004144.

Hainzl, S., Fischer, T., and Dahm, T.: Seismicity-based estimation of the driving fluid pressure in the case of swarm activity in Western Bohemia, *Geophys. J. Int.,* **191**(1), (2012), 271–281.

Hildreth, W.: Volcanological perspectives on Long Valley, Mammoth Mountain, and Mono Craters: Several contiguous but discrete systems, *J. Volcanol. Geothermal. Res.*, **136**(3), (2004), 169-198, doi: 10.1016/j.jvolgeores.2004.05.019.

Hill, D.P.: A model for earthquake swarms, *Journal of Geophysical Research*, **82**, (1977), 1347-1352, doi: 10.1029/JB082i008p01347.

Hill, D.P.: Temperatures at the base of the seismogenic crust beneath Long Valley Caldera, California, and the Phlegrean Fields Caldera, Italy, In: *Volcanic Seismology*, P. Gasparini, R. Scarpa, and K. Aki (eds.), Springer-Verlag, Berlin, (1992), doi: 10.1007/978-3-642-77008-1.

Hill, D.P.: Unrest in Long Valley Caldera, California, 1978-2004, *Geol. Soc. London Spec. Publ.*, **269**(1), (2006), 1-24.

Hill, D.P., and Prejean, S.: Magmatic unrest beneath Mammoth Mountain, California, *J. Volcanol. Geotherm. Res.*, **146**(4), (2005), 257-283, doi: 10.1016/j.jvolgeores.2005.03.002.

Hill, D.P., Langbien, J.O., and Prejean, S.: Relations between seismicity and deformation during unrest in Long Valley Caldera, California, from 1995 through 1999, *J. Volcanol. Geotherm. Res.*, **127**(3), (2003), 175-193, doi: 10.1016/S0377-0273(03)00169-0.

Hurd, O., and Zoback, M.D.: Regional stress orientations and slip compatibility of earthquake focal mechanism planes in the New Madrid Seismic Zone, *Seismological Research Letters*, **83**(4), (2012), 672-679, doi: 10.1785/0220110122.

Jeffrey, R., Zhang, X., and Jung, R.: Reassessing stimulation for EGS reservoirs, *Proceedings*, World Geothermal Congress, Melbourne, Australia, (2015).

Karimi-Fard, M., Durlofsky, L.J., and Aziz, K.: An efficient discrete-fracture model applicable for general-purpose reservoir simulators, *SPE Journal*, **9**(02), (2004), 227-236, doi: 10.2118/88812-PA.

Martínez-Garzón, P., Kwiatek, G., Ickrath, M. and Bohnhoff, M.: MSATSI: A MATLAB package for stress inversion combining solid classic methodology, a new simplified user-handling, and a visualization tool, *Seismological Research Letters*, **84**(4), (2014), 896-904, doi: 10.1785/0220130189.

McClure, M.W.: Generation of large postinjection-induced seismic events by backflow from dead-end faults and fractures, *Geophysical Research Letters*, **42**, (2015), 6647-6654, doi: 10.1002/ 2015GL065028.

McClure, M.W., Babazadeh, M., Shiozawa, S., and Huang, J.: Fully coupled hydromechanical simulation of hydraulic fracturing in three-dimensional discrete fracture networks, *SPE Journal*, **21**(04), (2016), 1302-1320, doi: 10.2118/173354-PA.

McClure, M.W., and Horne, R.N.: *Discrete Fracture Network Modeling of Hydraulic Stimulation: Coupling Flow and Geomechanics*, Springer Briefs in Earth Sciences, doi: 10.1007/978-3- 319-00383-2.

McClure, M.W., and Horne, R.N.: An investigation of stimulation mechanisms in Enhanced Geothermal Systems, *International Journal of Rock Mechanics & Mining Sciences*, **72**, (2014), 242-260, doi: 10.1016/j.ijrmms.2014.07.011.

Michael, A.J.: Determination of stress from slip data: faults and folds, *Journal of Geophysical Research: Solid Earth*, **89**(B13), (1984), 11517-11526, doi: 10.1029/JB089iB13p11517.

Michael, A.J.: Use of focal mechanisms to determine stress: A control study, *Journal of Geophysical Research: Solid Earth*, **92**(B1), (1987), 357-368, doi: 10.1029/JB092iB01p00357.

Montgomery-Brown, E.K., Wicks, C.W., Cervelli, P.F., Langbein, J.O., Svarc, J.L., Shelly, D.R., Hill, D.P., and Lisowski, M.: Renewed inflation of Long Valley Caldera, California (2011 to 2014), *Geophysical Research Letters*, **42**, (2015), 5250-5257, doi: 10.1002/2015GL064338.

Norbeck, J.H.: Hydromechanical and frictional faulting response of fluid-injection-induced earthquakes, Ph.D. thesis, Stanford University, Stanford, California, USA, (2016).

Norbeck, J.H., and Horne, R.N.: Evidence for a transient hydromechanical and frictional faulting response during the 2011 Mw 5.6 Prague, Oklahoma earthquake sequence, *Journal of Geophysical Research: Solid Earth*, **121**(12), (2016), 8688-8705, doi: 10.1002/2016JB013148.

Norbeck, J.H., and Horne, R.N.: A numerical method for fractured reservoir poromechanics using a mixed-continuum embedded fracture model, *Proceedings*, Geothermal Resources Council Transactions, **40**, Sacramento, California, USA, (2016).

Norbeck, J.H., and Horne, R.N.: Maximum magnitude of injection-induced earthquakes: A criterion to assess the influence of pressure migration along faults, *Tectonophysics*, (2018), accepted 23 January.

Norbeck, J.H., McClure, M.W., and Horne, R.N.: Field observations at the Fenton Hill enhanced geothermal system test site support mixed-mechanism stimulation, *Geothermics*, (2018), in review.

Norbeck, J.H., McClure, M.W., and Horne, R.N.: Revisiting stimulation mechanism at Fenton Hill and an investigation of the influence of fault heterogeneity on the Gutenberg-Richter b-value for rate-and-state earthquake simulations, *Proceedings*, 41st Workshop on Geothermal Reservoir Engineering, Stanford University, Stanford, California, USA, (2016), 1-22.

Norbeck, J.H., McClure, M.W., and Horne, R.N.: Analysis of hydromechanical reservoir response during fluid circulation at the Fenton Hill Enhanced Geothermal System test site, *Proceedings*, 38th New Zealand Geothermal Workshop, Auckland, New Zealand, (2016).

Norbeck, J.H., McClure, M.W., Lo, J.W., and Horne, R.N.: An embedded fracture modeling framework for simulation of hydraulic fracturing and shear stimulation, *Computational Geosciences*, **20**(1), (2016), 1-18, doi: 10.1007/s10596-015-9543-2.

Norbeck, J.H., and Rubinstein, J.L.: Hydromechanical earthquake nucleation model forecasts onset, peak, and falling rates of induced seismicity in Oklahoma and Kansas, *Geophysical Research Letters*, in review.

Okada, Y.: Internal deformation due to shear and tensile faults in a half-space, *Bulletin of the Seismological Society of America*, **82**(2), (1992), 1018-1040.

Olson, J.: Fracture aperture, length and pattern geometry development under biaxial loading: a numerical study with applications to natural, cross-jointed systems, In: *The Relationship between Damage and Localization*, Lewis, H., and Couples, G.D. (eds.), Geological Society, London, Special Publications, The Geological Society of London, (2007), 123-142, doi: 10.1144/SP289.8.

Segall, P.: *Earthquake and Volcano Deformation*, Princeton University Press, (2010).

Schoenball, M., and Ellsworth, W.L.: A systematic assessment of the spatiotemporal evolution of fault activation through induced seismicity in Oklahoma and Kansas, Journal of Geophysical Research: Solid Earth, 122(12), (2017), 10189-10206, doi: 10.1002/2017JB014850.

Shelly, D.R., Ellsworth, W.L., and Hill, D.P.: Fluid-faulting evolution in high definition: Connecting fault structure and frequency-magnitude variations during the 2014 Long Valley Caldera, California, earthquake swarm, *Journal of Geophysical Research: Solid Earth*, **121**, (2016a), 1776-1795, doi: 10.1002/2015JB012719.

Shelly, D.R., Hardebeck, J.L., Ellsworth, W.L., and Hill, D.P.: A new strategy for earthquake focal mechanisms using waveform-correlation-derived relative polarities and cluster analysis: Application to the 2014 Long Valley Caldera earthquake swarm, *Journal of Geophysical Research: Solid Earth*, **121**, (2016b), 8622-8641, doi: 10.1002/2016JB013437.

Shelly, D.R., Moran, S.C., and Thelen, W.A.: Evidence for fluid-triggered slip in the 2009 Mount Rainier, Washington earthquake swarm, *Geophysical Research Letters*, **40**, (2013) 1506–1512, doi:10.1002/grl.50354.

Sibson, R. H.: Earthquake rupturing as a mineralizing agent in hydrothermal systems, *Geology*, **15**(8), (1987), 701–704, doi: 10.1130/0091-7613(1987)15<701:ERAAMA>2.0.CO;2.

Sibson, R.H.: Structural permeability of fluid-driven fault-fracture meshes, *Journal of Structural Geology*, **18**(8), (1996), 1031-1042, doi: 10.1016/0191-8141(96)00032-6.

Townend, J., and Zoback, M.D.: How faulting keeps the crust strong, *Geology*, **28**(5), (2000), 399-402, doi: 10.1130/0091-7613(2000)28<399:HFKTCS>2.0.CO;2.

Waldhauser, F., and Ellsworth, W.L.: A double-difference earthquake location algorithm: Method and application to the northern Hayward fault, California, *Bulletins of the Seismological Society of America*, **90**(6), (2000), 1353-1368, doi: 10.1785/0120000006.

Walsh, F.R., and Zoback, M.D.: Probabilistic assessment of potential fault slip related to injection-induced earthquakes: Application to north-central Oklahoma, USA, *Geology*, **44**(12), (2016), 1-4, doi: 10.1130/G38275.1.

Willis-Richards, J., Watanabe, K., and Takahashi, H.: Progress toward a stochastic rock mechanics model of engineered geothermal systems, *Journal of Geophysical Research: Solid Earth*, **101**(B8), (1996), 17481-17496, doi: 10.1029/96JB00882.

Witherspoon, P., Wang, J. Iwai, K., and Gale, J.: Validity of cubic law for fluid flow in a deformable rock fracture, *Water Resources Research*, **16**(6), (1980), 1016-1024, doi: 10.1029/WR016i006p01016.

Zhang, X., and Jeffrey, R.: Fluid-driven nucleation and propagation of splay fractures from a permeable fault, *Journal of Geophysical Research: Solid Earth*, **121**, (2016), 1016-1024, doi: 10.1002/2016JB013304.

Zaliapin, I., and Ben-Zion, Y.: Earthquake clusters in southern California II: Classification and relation to physical properties of the crust, *Journal of Geophysical Research: Solid Earth*, **118**, (2013), 2865-2877, doi: 10.1002/jgrb.50178.

Zoback, M.D.: *Reservoir Geomechanics*, Cambridge University Press, (2007).